

Plasma-target surface interaction during non-equilibrium plasma irradiation at atmospheric pressure: Generation of dusty plasma

LIMIN LI,¹ CHAO LIU,^{1,2} XUMING ZHANG,¹ GUOSONG WU,¹ MING ZHANG,¹ RICKY K.Y. FU,¹
AND PAUL K. CHU¹

¹Department of Physics and Materials Science, City University of Hong Kong, Kowloon, Hong Kong, China

²School of Electronics Science, Northeast Petroleum University, Daqing, China

(RECEIVED 18 March 2013; ACCEPTED 15 October 2013)

Abstract

The remaining challenges, developing the relativistic electron beam sources, stimulate the investigations of cathode materials. Carbon-fiber-aluminum composite is the most appropriate cathode materials to construct the robust relativistic electron beam sources. Carbon-fiber-aluminum composite is treated by a non-equilibrium atmospheric plasma torch with a copper electrode based on high-voltage gas discharge. The axial and radial distributions of the plasma torch temperature are measured to determine the optimal treatment temperature and location. Copper-oxide particles with diameters of less than 1 μm are deposited onto the surface of the carbon-fibers and a layer of copper-oxide covers the entire surface as the treatment time is increased. Raman spectroscopy suggests that although the locations of the D and G band are similar, the areas of the D and G bands increase after the plasma treatment due to the reduced graphite crystalline size in the carbon-fibers. Analysis of the copper electrode surface discloses materials ablation arising from the discharge which releases copper from the source. Our results reveal that the atmospheric plasma torch generated by high-voltage discharge is promising in the surface modification of the carbon-fiber-reinforced aluminum composite. Further, the plasma produced by atmospheric plasma torch is dusty plasma, due to the participation of liberated copper particles. The plasma torch was analyzed by fluid dynamics, in terms of plasma density, plasma expansion velocity, and internal pressure, and it was found that the plasma produced by atmospheric torch is supersonic flow.

Keywords: Aluminum composite; Atmospheric plasma; Dusty plasma

INTRODUCTION

To develop the relativistic electron beam sources, the cathode materials are the key factor, and carbon-fiber cathode has been an appropriate candidate to generate electron beam (Cheng *et al.*, 2013; Fan *et al.*, 2013; Liu *et al.*, 2012; Peng *et al.*, 2011; Shao *et al.*, 2012; Teng *et al.*, 2013; Zhang *et al.*, 2013a; 2013b; 2012b). Carbon-fibers are usually utilized to reinforce composite materials due to their superior mechanical properties such as high specific strength modulus, low expansion coefficient, small density, good environmental compatibility, long-term durability, and high resistance to chemical corrosion (Li *et al.*, 2009a;

Pan *et al.*, 2010; Tiwari *et al.*, 2011). Carbon-fibers are used in vacuum electronic tubes because this type of high-current electron beam source typically has a long life-time and low work function while producing a uniform plasma across the cathode surface at a small plasma expansion velocity (Li *et al.*, 2012; 2011; 2009c; 2009d). By combining CsI with carbon-fibers, strong plasmas can be generated from the cathode surface under slower plasma expansion while the diode gap during the main voltage pulse is almost unchanged (Li *et al.*, 2009b). Additionally, the carbon-fibers can be subjected to different types of surface modification, for example, chemical and thermal processes, electron beam irradiation, and ultrasonic bombardment (Nohara *et al.*, 2005). It has been observed that plasma treatments can enhance the roughness and adsorption ability of the fiber surface and some polar groups can be introduced onto the fiber surface (Kolb *et al.*, 2012).

Address correspondence and reprint requests to: Paul K. Chu, Department of Physics and Materials Science, City University of Hong Kong, Tat Chee Avenue, Kowloon, Hong Kong, China. E-mail: paul.chu@cityu.edu.hk

An atmosphere plasma produced by dielectric barrier discharge or radio-frequency discharge can be used to modify carbon-fibers and non-thermal atmospheric plasmas have received increasing attention in surface and materials processing, especially pertaining to biomedical engineering (Kolb *et al.*, 2012). Compared to conventional plasma systems confined in a vacuum chamber, non-thermal atmospheric plasmas have advantages such as lower operating cost, smaller equipment cost-of-ownership, and production of abundant radical species (Lu *et al.*, 2008a). Atmospheric plasma torches, one type of non-thermal atmospheric plasma sources, are capable of generating plasmas in open space rather than in a discharge gap (Lu *et al.*, 2008a). The atmospheric plasma torches are flexible, compact, and efficient (Lu *et al.*, 2008b), thereby rendering direct treatment of large samples relatively straightforward. Plasma torches are commonly generated by direct-current micro-hollow cathode discharge, high-frequency dielectric barrier discharge, radio-frequency inductively-coupled microwave discharge, as well as radio and microwave coupled discharge (Sarani *et al.*, 2011; UGent *et al.*, 2011; Wu *et al.*, 2011; 2012; Yan *et al.*, 2009; Yousfi *et al.*, 2012; Zhang *et al.*, 2012a).

Although carbon-fiber reinforced aluminum composites have been processed by high-current pulsed electron beams (Li *et al.*, 2009d), the use of non-thermal atmospheric plasma torch is not as common and the mechanism of surface property enhancement is not well understood. In this work, the efficacy of the non-thermal atmospheric plasma torch treatment of carbon-fiber reinforced aluminum composite is investigated. The non-thermal plasma torches are produced between two coaxial electrodes separated by a small gap. A pulsed high voltage is applied to the inner electrode whereas the outer electrode is grounded. The untreated and treated materials are characterized systematically by scanning electron microscopy (SEM), energy-dispersive X-ray spectroscopy (EDS), and Raman spectroscopy.

EXPERIMENTAL DETAILS

Figure 1a depicts the schematic of the non-thermal plasma device operated at atmospheric pressure. The device includes three main sections, a power supply or high voltage generator

to produce the high voltage, gas injection system, and gas discharge system. The high voltage generator consists of a transformer and modulator, and the generated high voltage of 10–50 kV is applied to the copper electrode of the plasma device. The copper electrode which serves as the anode has a diameter of 2 mm and length of 100 mm. The length, inner diameter, and outer diameter of the stainless steel tube are 87 mm, 20 mm, and 30 mm, respectively. The copper electrode is located at the axis of the stainless steel tube. As shown in Figure 1, the stainless steel cone is connected to the right end of the tube and the left end of the tube is sealed by an insulator made of a macromolecular polymer. The tip of the cone is open and the interval between the hole and right end of the tube is 15 mm. The tube and cone constitute the shell of the chamber for the gas discharge.

In the experiments, nitrogen was bled into the chamber *via* the inlet at the side of the chamber to produce the discharge. The shell of the chamber was grounded by copper wires. The gas discharge triggered between the gaps of the two electrodes produced the gas plasma in the gap if the chamber was fully sealed. However, as a result of the gas flow, the gas plasma generated at atmospheric pressure was transported from the gap between the two electrodes through the small hole at the end of the chamber. Figure 1b presents a visual illustration of the interaction between the atmospheric plasma torch and sample. Figure 2 shows the dependence of current and voltage of plasma torch discharge. Here the current and voltage are measured by changing the resistance connected with torch outer shield and ground. One can see that the discharge current remained at the order of milliamperes, and increased with the applied voltage.

The carbon-fiber-reinforced aluminum composite was produced by the squeeze casting technique. The carbon-fibers had a temperature range of 300 to 3 K and the diameter of the fibers was 5 μm . By using 99.95% nitrogen at 700°C under 10 PA, the epoxy layer was removed from the carbon-fibers which were then stretched in the fixed direction. The fibers were placed in a stainless steel tube on a crucible. An aluminum melt was incorporated into the carbon fibers by a squeeze machine. After cooling, the carbon-fiber-reinforced aluminum composite was produced.

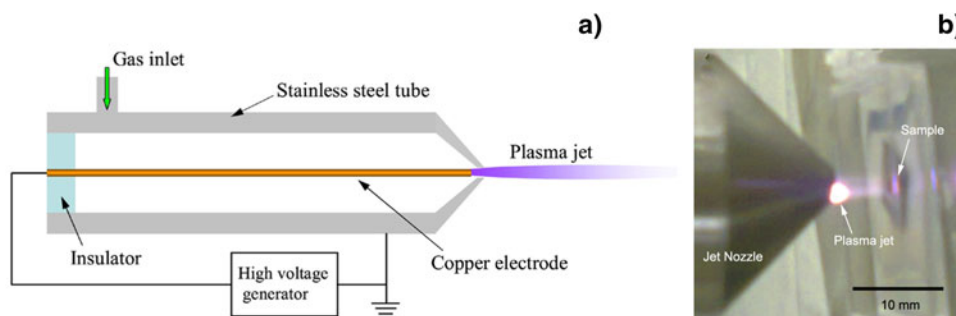


Fig. 1. (Color online) (a) Schematic of the non-thermal nitrogen plasma torch at atmosphere pressure, including the high-voltage generator, insulator, copper electrode, stainless steel tube, and gas inlet. (b) Photograph of the plasma torch nozzle interacting with the sample.

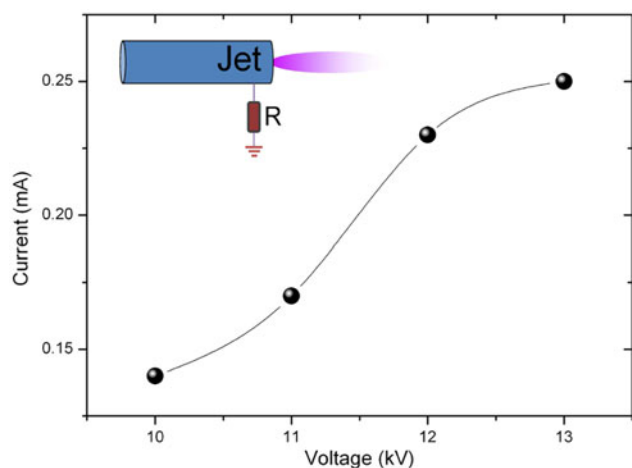


Fig. 2. (Color online) Current versus voltage of plasma torch discharge.

RESULTS AND ANALYSIS

The plasma torch is transported from the discharge by the flowing gas through this discharge channel. This distance between the copper electrode and nozzle opening defines the gap between the electrodes and is fixed at 1 mm. The gas discharge occurs in the small gap and the electric field in the gap between the two electrodes is on the order of 10^7 V/m. It should be pointed out that this is the externally applied electric field, but the microscopic electric field on the surface of the tip of the copper electrode can exceed the externally applied electric field. The diameter of the nozzle opening is 3 mm which is critical to the operation of the gas discharge and generation of the plasma torch. The diameter of nozzle opening affects the radial dimension of the plasma torch. A significant part of the energy produced by the discharge results in heating and increases the temperature of the expelled plasma torch. Figure 3 presents the time evolution of the

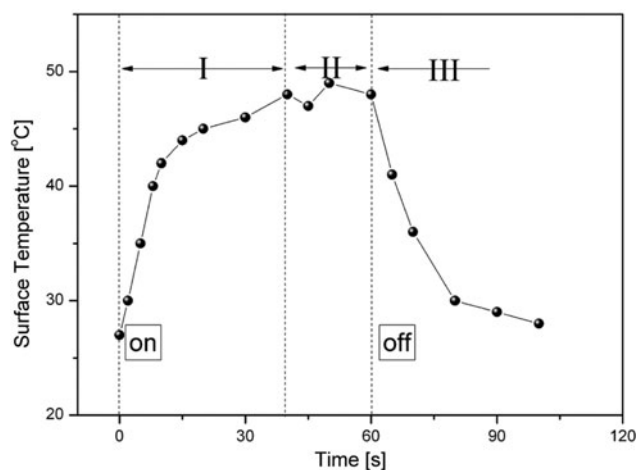


Fig. 3. Relationship of surface temperature of the thermal probe versus measurement time as the plasma torch is being switched on and off with the distance between the opening of the plasma torch nozzle and surface of thermal probe being 8 mm (room temperature = 27°C).

surface temperature of the thermal probe used to detect the atmospheric plasma torch. The thermal probe is located at an axial distance of 8 mm and the axis center of the plasma torch. The surface temperature of the thermal probe increases to 48°C within 40 s after the plasma torch is turned on and then stabilizes. After the plasma torch is turned off, the surface temperature of the thermal probe decreases rapidly back to room temperature. The axial and radial distributions of the plasma torch temperature can be measured by adjusting the position of the thermal probe relative to the nozzle opening.

Figure 4 shows the effect of gas flow rate on the length of plasma jet. It can be observed that the maximum length of plasma jet occurs at the flow rate of about 3 l/min, and higher or lower flow rate will cause the reduction of plasma jet length. Therefore, the flow rate of argon gas remains at about 3 l/min during the experiments of surface treatment of carbon fiber. The plasma torch with a luminous plume of around 15 mm in length is expelled from the discharge channel as shown in Figure 1b. The temperature distribution versus distance from the nozzle opening is presented in Figure 5a. The temperature is recorded by a thermal probe and room temperature is 27°C. As the axial distance d from the nozzle opening is increased to 6 mm, the temperature of the plasma torch increases from 36°C at $d = 1.5$ mm to around 47°C at $d = 6$ mm. For $6 \text{ mm} < d < 8$ mm, the temperature of plasma torch is around 47°C, whereas for $8 \text{ mm} < d < 12.5$ mm, the temperature diminishes from 47°C to 40°C. For $12.5 \text{ mm} < d < 22$ mm, the temperature of plasma torch remains at around 40°C, but when the distance exceeds 22 mm, the temperature of plasma torch begins to decrease again. Some plastic or biological samples are prone to damage at high temperature. For example, if cellular materials are subjected to a temperature a few degrees higher than the ambient one, the cellular materials may suffer irreparable damage. In the case of plasma treatment of cellular materials, the proper temperature

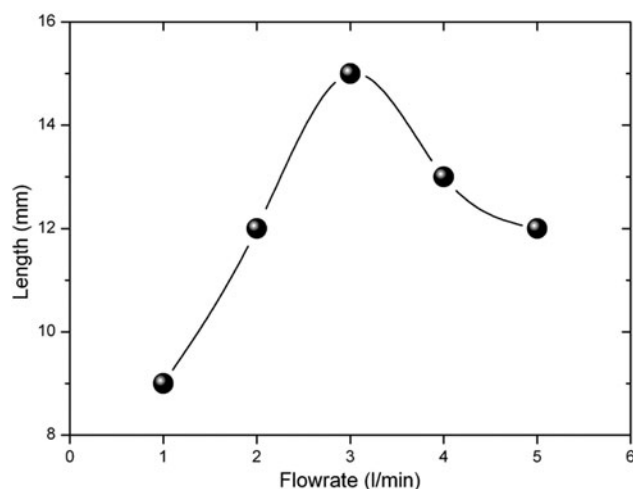


Fig. 4. Effect of argon flow rate on the length of plasma jet.

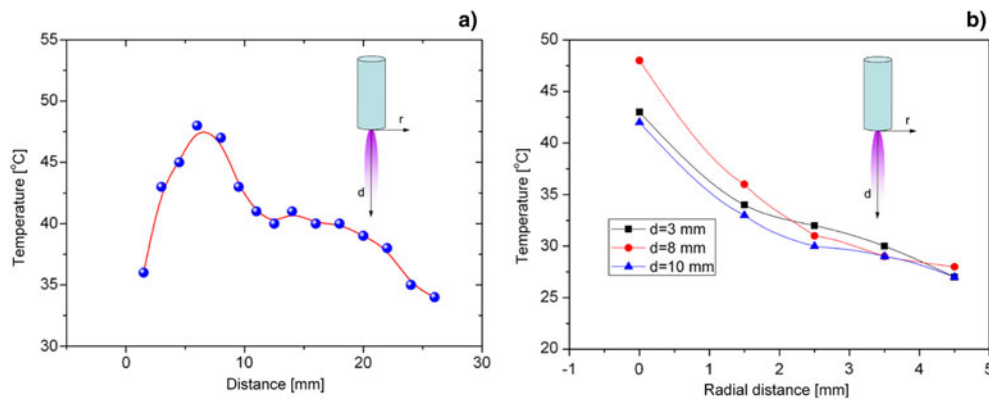


Fig. 5. (Color online) Temperature distribution of the atmospheric plasma torch: (a) Along the axial direction and (b) Along the radial direction. The temperature data are obtained by a thermal probe. The operating gas is nitrogen and room temperature is 27°C.

can be achieved by adjusting the axial position of the sample relative to the nozzle opening. Hence, the axial distribution of the plasma torch is very important and determines the appropriate location of the sample. In our experiments, the visible length of the plasma torch is about 15 mm and according to the axial distribution of plasma torch, the effective length of the plasma torch is estimated to be over 20 mm, as shown in Figure 5a. In the plasma treatment of the carbon-fiber-reinforced aluminum composite, the axial distance of sample relative to the nozzle opening is selected to be 8 mm corresponding to the maximum allowable

temperature. The radial distribution of the plasma torch temperature at different distances is presented in Figure 5b. Regardless of the axial distance, the plasma torch temperature decreases to below 37°C at 1.5 mm off the axis of the plasma torch and remains at over 30°C until the radial distance exceeds 2.5 mm. The visible radius of the plasma torch is about 1.5 mm which is possibly limited by the geometric diameter (3 mm) of the nozzle opening. Actually, the radius of the plasma torch should at least exceed the visible radius of the plasma torch due to radial diffusion of the ions and it determines the effective area exposed to the

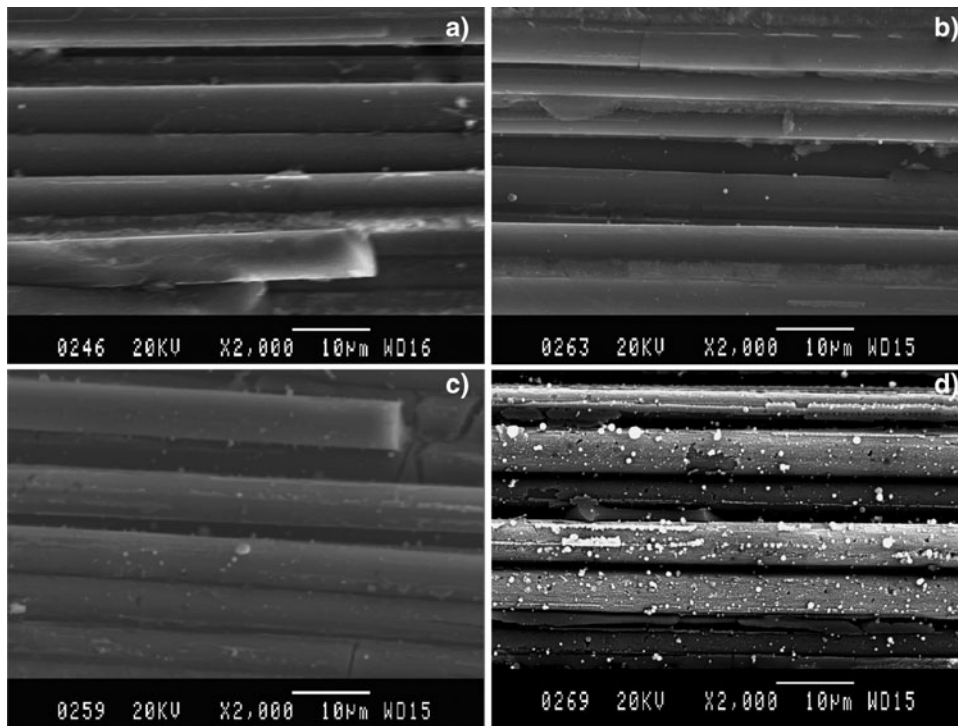


Fig. 6. SEM images of the untreated and treated surfaces of the carbon-fiber-reinforced aluminum composite at an amplification factor of 2000: (a) Untreated sample, (b) Sample treated by the plasma torch for 15 min, (c) Sample treated by the plasma torch for 30 min, and (d) Sample treated by the plasma torch for 60 min. The axial distance of the sample surface from the nozzle opening is 8 mm and the gas is nitrogen.

plasma torch and extent of interaction between the plasma torch and sample surface.

Figure 6a presents the SEM image of the surface of the carbon-fiber-reinforced aluminum composite untreated by the nitrogen atmospheric plasma torch. As shown by the side view, some fillings composed of possibly aluminum or aluminum-oxide are distributed among the fiber gaps. These fillings link the carbon-fibers and produce excellent electrical or mechanical connection between the fibers to potentially increase the hardness of the materials. Here, the carbon-fiber-reinforced aluminum composite is placed at the axial center of plasma torch at a distance of 8 mm at which the temperature of the nitrogen atmospheric plasma torch is around 47°C based on the results shown in Figure 5. After plasma processing for 15 min, small quantities of particles several hundreds of nanometers in size having a non-uniform distribution can be observed from Figure 6b. The carbon-fibers have a smaller amount of scraps compared to the original surface, indicating that the plasma torch cleans and smooth the surface. As the plasma processing time increases, the number of particles goes up, as shown in Figure 6c. The surface of the carbon-fibers begins to roughen after 30 min and after 60 min, the density, size, and amount of particles increase obviously, as shown in Figures 6b and 6d. Some deposited materials produced by the plasma torch also appear on the carbon-fibers.

To further determine the surface characteristics of carbon-fiber-reinforced aluminum composite treated by nitrogen atmospheric plasma torch, Figure 7a depicts the SEM micrograph of the surface of the carbon-fibers after plasma treatment for 15 min. Many particles with diameters of less than 1 μm are observed from the surface and some particles are as small as 100 nm. The EDS results (inset in Fig. 7a) reveal that the particles are composed of copper-oxide. The apparent source of copper is the copper electrode. Figure 7b shows the SEM image of fibers after plasma treatment for 30 min and a layer of copper-oxide is observed although the surface is still not totally covered. As the surface treatment time is increased further, the surface is finally covered entirely by copper-oxide, as shown in Figure 7c. Figure 7d shows the magnified surface of the treated carbon-fiber in Figure 7c disclosing many scraps among the particles. Furthermore, the particles are not spherical like the ones in Figure 7a and these particles are clusters of copper-oxide. It should be pointed out that the lack of copper-nitride on the surface of carbon-fiber may be due to the rapid decomposition of copper nitride by heating in air.

The structural changes in the carbon-fiber-reinforced aluminum composite before and after the plasma torch treatment are determined by Raman spectroscopy which is a useful tool to discern the ordered and disordered crystalline structures of carbon. Graphitic carbon and other sp^2

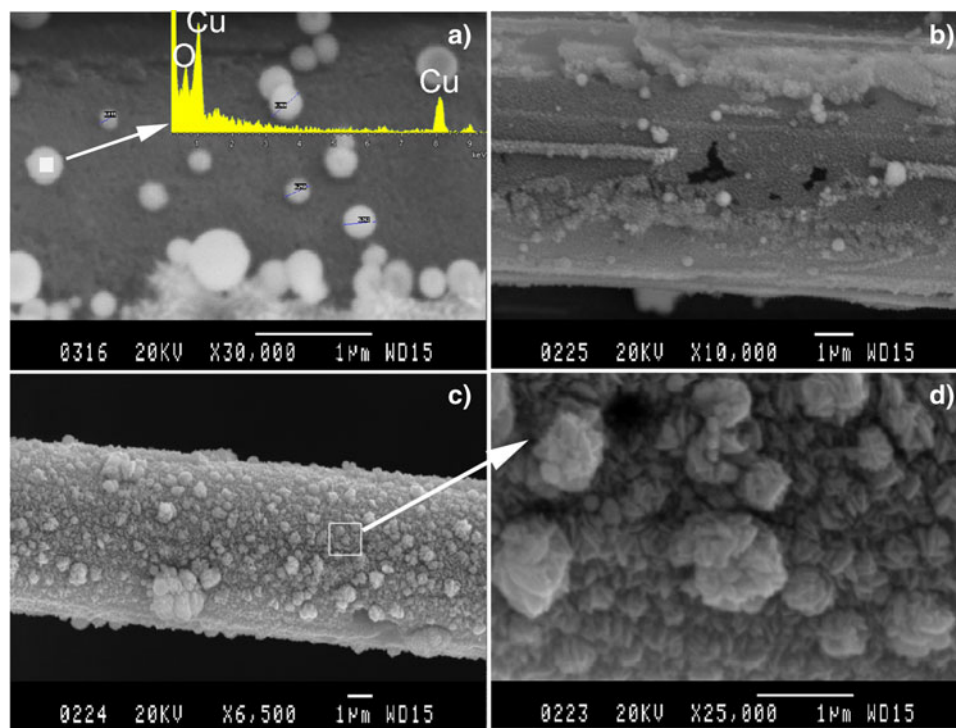


Fig. 7. (Color online) SEM images: (a) Carbon-fiber-reinforced aluminum composite treated by the plasma torch for 15 min (30,000 \times) with the inset being the EDS spectrum, (b) Sample treated by the plasma torch for 30 min (10,000 \times), (c) Sample treated by the plasma torch for 60 min (6,500 \times), and (d) Sample treated by the plasma torch for 60 min (25,000 \times). The axial distance between the sample surface and nozzle opening is 8 mm and the plasma gas is nitrogen.

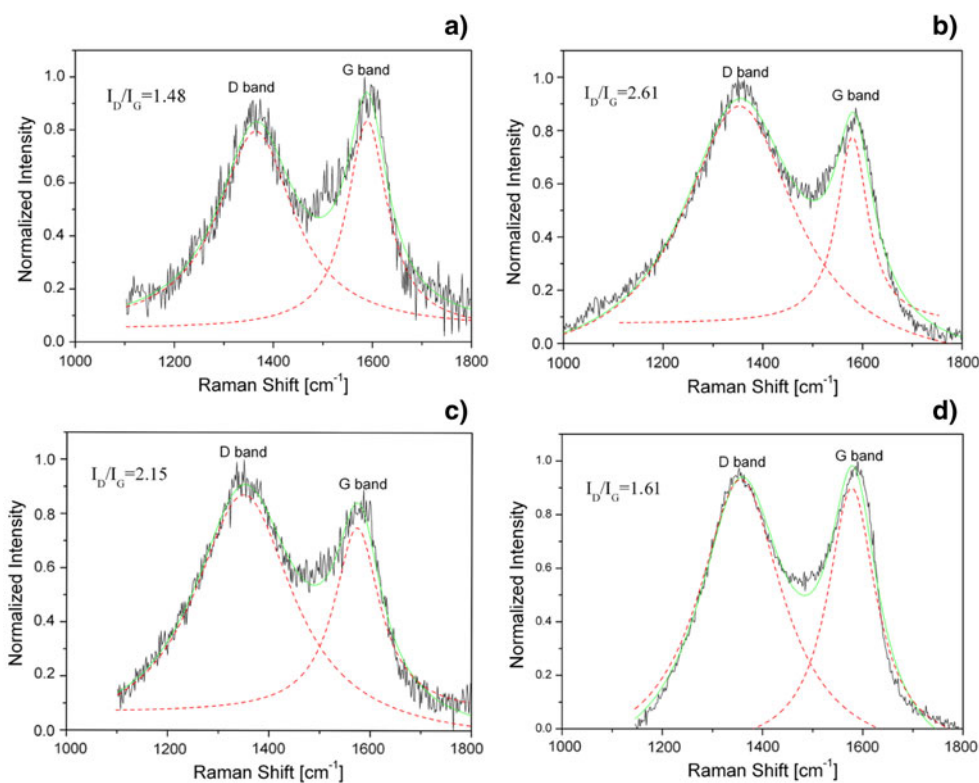


Fig. 8. (Color online) Raman spectra acquired from the carbon-fiber-reinforced aluminum composite: (a) Untreated sample (reference), (b) Sample treated by the plasma torch for 15 min, (c) Sample treated by plasma torch for 30 min, and (d) Sample treated by plasma torch for 60 min.

bonded amorphous carbons exhibit strong Raman scattering thus providing useful information about the phases and structural changes in the materials. The carbon-fiber-reinforced composite shows one apparent peak at about 1589 cm^{-1} (G band) and another apparent peak at about 1363 cm^{-1} (D band) prior to the plasma treatment, as shown in Figure 8a. The G band arises from all sp^2 bonds of graphite due to the vibrational mode of E_{2g} whereas the G band corresponds to the sp^2 bonds in the broken aromatic rings of disorder graphite due to the A_{1g} vibration mode (Nohara *et al.*, 2005). The ratio of the D and G bands (I_D/I_G) can be regarded as a measure of the crystalline order of carbon materials. The I_D/I_G values are derived from the Raman data using the Lorentzian function based on the ratio of the areas of the D and G bands. As shown in Figure 8a, I_D/I_G is calculated to be 1.48 for the untreated carbon-fiber-reinforced aluminum composite. After plasma treatment for 15 min, the D band and G band are located at 1353 cm^{-1} and 1579 cm^{-1} , respectively and the I_D/I_G value is 2.61, as shown in Figure 8b. After 30 min of plasma treatment, the D and G bands are at 1350 cm^{-1} and 1570 cm^{-1} , respectively and I_D/I_G is 2.15, as shown in Figure 8c. After 60 min, the locations of the D and G bands are 1354 cm^{-1} and 1584 cm^{-1} , respectively and I_D/I_G is 1.61, as shown in Figure 8d. Hence, the band locations are similar for the untreated and treated samples, but the I_D/I_G ratios are different. The I_D/I_G ratio increases after the plasma treatment but among the treated samples, the ratio decreases with treatment time.

The graphite crystalline size L_a is equal to $C/(I_D/I_G)$, where $C = 4.4\text{ nm}$ (Nohara *et al.*, 2005). Figure 9 presents the surface crystalline size of the untreated and treated samples. After treatment for 15 min, the graphite crystalline size decreases from about 3 nm to about 1.7 nm. As the treatment time increases, the graphite crystalline size increases to about 2.7 nm, but on a whole, after the surface treatment, the graphite crystalline size becomes smaller than that of the untreated materials. The trend reflects the alterations in the

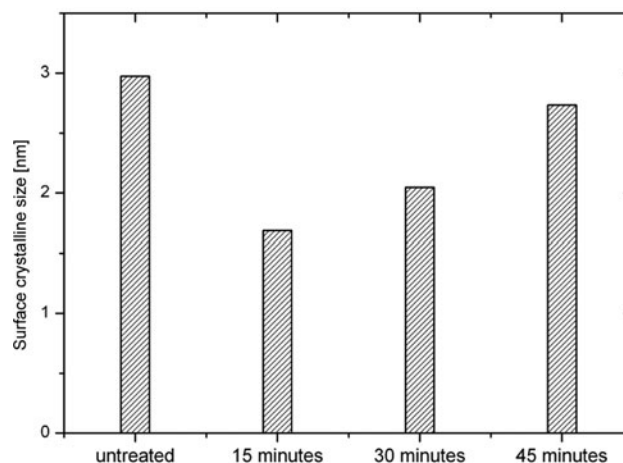


Fig. 9. Comparison of crystalline size of untreated and treated carbon fibers after plasma treatment for different durations.

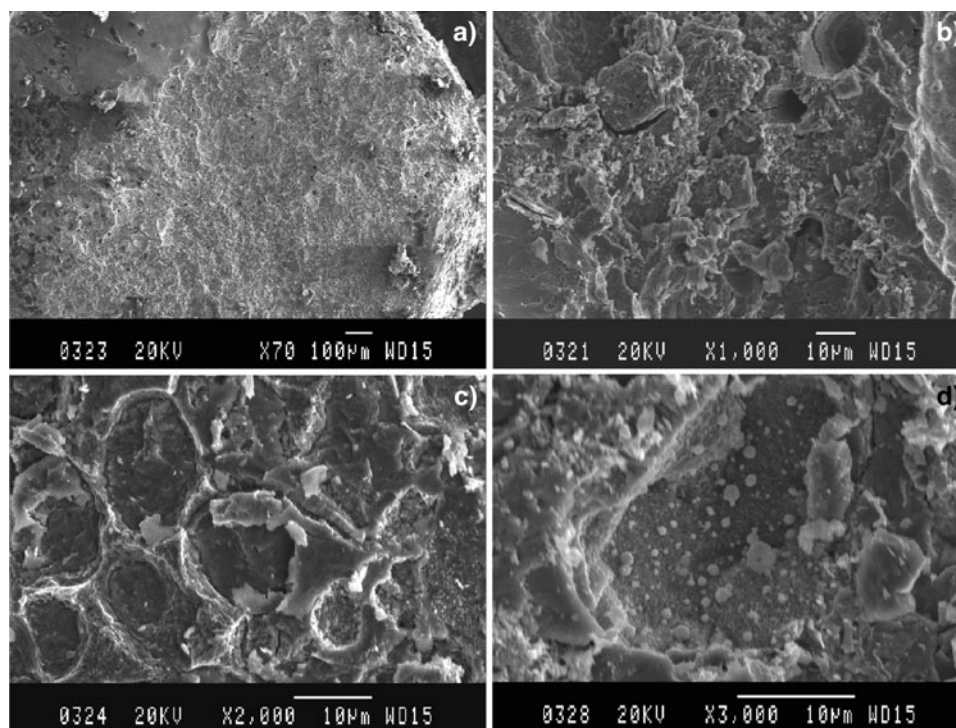


Fig. 10. SEM images of corroded surface on the copper electrode after gas discharge at different magnifications: (a) 70 \times , (b) 1,000 \times , (c) 2,000 \times , and (d) 3,000 \times .

ordering of the graphitic structures. The smaller graphite crystalline size after the plasma surface treatment indicates less ordering of the graphitic structures compared to the untreated sample. Furthermore, as the treatment time increases, the larger graphite crystalline size shows more ordering of the graphitic structures. To reduce the graphite crystalline size in the carbon-fibers, it is necessary to control the treatment time.

To further investigate the deposition mechanism, the surface of the copper electrode is examined by SEM. Figure 10 depicts the SEM micrographs of the corroded surface on the copper electrode after the gas discharge. The surface is obviously damaged as shown in Figure 10a. Figures 10b and 10c further disclose the presence of craters and fragments on the copper electrode. As shown in Figure 10c, adjacent craters form honeycombs and the lateral dimension of these craters is about 10 μm . The fragments and craters are distributed randomly on the corroded surface and particles with diameters of several micrometers can be observed from the craters in Figure 10d. Formation of fragments, craters, and particles is closely related to the ablation process on the electrode. For metal electrodes, the high-voltage discharge characteristics are dictated by the craters and microprotrusions. The edge between adjacent craters forms microprotrusions from which ejection of electrode materials arises. As the high-voltage discharge continues, the microprotrusions disappear gradually and the craters become larger. The ejected electrode materials lead to the formation of the particles in the craters shown in Figure 10d. Therefore,

deposition of copper onto the surface arises from ablation of the copper electrode during high-voltage gas discharge.

DISCUSSIONS

Carbon-fiber-reinforced aluminum composite samples prepared by squeeze casting are treated by an atmospheric nitrogen plasma torch. The axial and radial distributions of the plasma temperature are determined in order to select the optimal treatment temperature and sample location. The maximum temperature is observed at an axial distance of 8 mm from the nozzle opening. SEM discloses the presence of particles on the plasma-treated materials and as the treatment time increases, the density and number of deposited particles go up. After 60 min, a continuous layer composed of copper-oxide is deposited onto the sample. Raman spectroscopy reveals that the D band and G band locations of the untreated and plasma-treated samples are similar but the area ratios are different. The areas of the D band and G band increase after the plasma treatment due to the reduced graphite crystalline size in the carbon-fibers. Analysis of the copper electrode surface reveals materials ablation from the discharge thereby releasing copper from the source. This plasma torch treatment is effective in altering the surface properties of carbon-fiber-reinforced aluminum composite.

Based on the experimental observations, the plasma generated by atmospheric plasma torch is dusty plasma in nature. Dusty plasma is an ionized gas containing small particles of solid matter, which become electrically charged, as

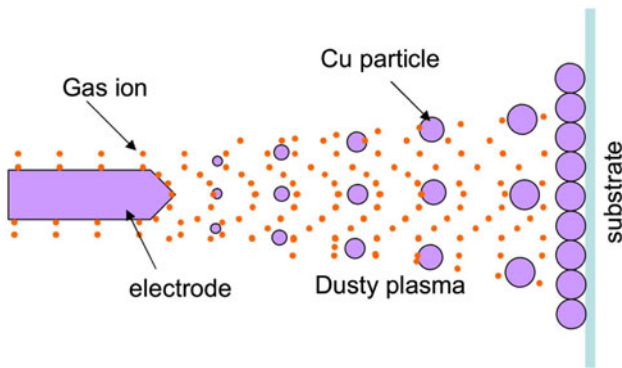


Fig. 11. (Color online) Dusty plasma produced by atmospheric plasma torch.

shown in Figure 11. Particles may be dielectric or conducting, and typically range from nanometer clusters to millimeter sizes. The interaction between a dust grain and the surrounding plasma is an extremely complicated two-way process. This interaction is the charging of the dust grain. The charge depends on the fluxes of ions and electrons from the plasma onto the grain surface. The charged grains will modify their plasma environments by setting up space charges and electrostatic fields. The dust plasma produced by atmospheric plasma torch is still rather poorly understood, and we need better understanding of it. Here, the dusty plasma is assumed to obey the fluid dynamics. According to the mass conservation equation, we can obtain

$$\frac{\partial(\rho v_Z)}{\partial Z} + \frac{1}{R} \frac{\partial(R\rho v_R)}{\partial R} = 0, \quad (1)$$

which is at cylindrical coordinates, and ρ is the mass density of plasma torch, v_Z is the axial velocity of plasma drift, v_R is the radial velocity of plasma drift. Thus, it can be transferred to be

$$\frac{\partial(\rho v_Z)}{\partial Z} + \frac{\partial(\rho v_R)}{\partial R} + \frac{\rho v_R}{R} = 0. \quad (2)$$

Here, the angular velocity of plasma drift is neglected, namely, $v_\phi = 0$. According to Bernoulli equation, we can obtain

$$dP = -\frac{\rho}{2} d(v_R^2 + v_Z^2). \quad (3)$$

Further, the ion-acoustic velocity C_s can be described as

$$C_s^2 = \frac{dP}{d\rho}, \quad (4)$$

where P is the internal pressure of dusty plasma torch. Thus,

$$d\rho = -\frac{\rho}{C_s^2} (v_R dv_R + v_Z dv_Z), \quad (5)$$

Additionally, the following equations can be considered,

$$\frac{\partial \rho}{\partial Z} = -\frac{\rho}{C_s^2} \left(v_R \frac{\partial v_R}{\partial Z} + v_Z \frac{\partial v_Z}{\partial Z} \right), \quad (6)$$

$$\frac{\partial \rho}{\partial R} = -\frac{\rho}{C_s^2} \left(v_R \frac{\partial v_R}{\partial R} + v_Z \frac{\partial v_Z}{\partial R} \right). \quad (7)$$

By the combination of the above equations, we can obtain

$$\left(1 - \frac{v_R^2}{C_s^2} \right) \frac{\partial v_R}{\partial R} - \frac{v_Z v_R}{C_s^2} \frac{\partial v_R}{\partial Z} - \frac{v_R v_Z}{C_s^2} \frac{\partial v_Z}{\partial R} + \left(1 - \frac{v_Z^2}{C_s^2} \right) \frac{\partial v_Z}{\partial Z} = -\frac{v_R}{R}. \quad (8)$$

For the dusty plasma torch with axial symmetry and non-rotation,

$$\frac{\partial v_R}{\partial Z} = \frac{\partial v_Z}{\partial R}. \quad (9)$$

Thus, we can obtain the following equation,

$$\left(1 - \frac{v_R^2}{C_s^2} \right) \frac{\partial v_R}{\partial R} - \frac{v_Z v_R}{C_s^2} \frac{\partial v_R}{\partial Z} - \frac{v_R v_Z}{C_s^2} \frac{\partial v_Z}{\partial R} + \left(1 - \frac{v_Z^2}{C_s^2} \right) \frac{\partial v_Z}{\partial Z} = -\frac{v_R}{R}. \quad (10)$$

Here, the axial velocity of plasma drift is assumed to be the ion-acoustic velocity C_s , $v_Z = C_s$, and the radial velocity of plasma expansion v_R is independent of Z . According to Eq. (10), the radial velocity of plasma expansion v_R can be obtained, as shown in Figure 12a. Based on Eq. (5) and the values of v_R and v_Z , the plasma density can be calculated, as shown in Figure 12b. In Figure 12c, the value of $\rho v^2/2$ is presented by using the values of plasma density and plasma expansion velocity. In Figure 12d, the pressure difference relative to the axial center of plasma jet ΔP is calculated by using Eq. (3) and the values of plasma density and plasma expansion velocity. Here, it should be pointed out that the results in Figure 12 are obtained under the conditions of different emitter radii or internal electrode radii. It was found from Figure 12a that the plasma expansion velocity grows with the increase in the distance from the emission center. Further, for the smaller emission radius, the plasma expansion velocity increased faster. In each case, rapidly increasing velocity occurs close to the emission center, which is followed by a slowly changed process. Most notably, the plasma torch with different emission radii is a supersonic flow. Figure 12b shows the distribution of relative plasma density. One can see that the plasma density fast decrease along the radial direction of plasma torch. Thus, a boundary between the emission zone and rarefaction plasma region is generated. Specially, at emission radius of 1 mm, the radius of plasma boundary can be estimated to be less than 2 mm.

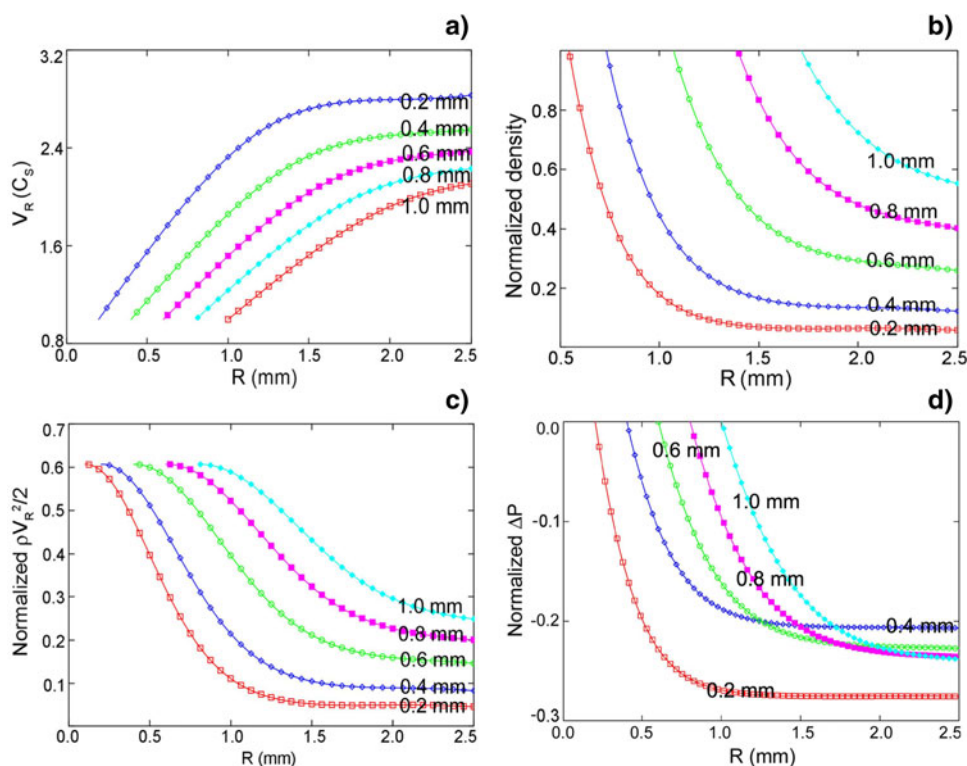


Fig. 12. (Color online) (a) velocity distribution of plasma expansion, (b) plasma density, (c) value of $\rho v^2/2$, and (d) pressure difference.

For the copper electrode of 2 mm diameter, namely, the radius of emission radius was 1 mm, the visible radius of plasma torch was about 1.5 mm. Thus, the calculated result agrees well with the experimental observation. From the values of $\rho v^2/2$ can be obtained for different emission radii in Figure 12c, one can see that in each case, the value of $\rho v^2/2$ from the peak to steady-state decreased at the distance of 1 mm from the emission center. Further, the pressure difference relative to the axial center of plasma torch is presented in Figure 12d. One can see that as the radius of emission center increased from 0.2 mm to 1 mm, the pressure difference grew faster and faster. That is, the plasma torch with a small emission radius will produce a low internal plasma pressure.

In this paper, the atmospheric plasma torch was applied to treat the surface of carbon-fiber-aluminum composite. It was found experimentally that the plasma produced by atmospheric plasma torch is dusty plasma, due to the generation of copper particles participating in the ejection process of plasma torch. Thus, the dusty plasma including copper particles induced the deposition of copper-oxide on the surface of carbon-fiber-aluminum composite. The plasma torch was analyzed by fluid dynamics, and it was found that the plasma can be controlled by adjusting the dimensions of internal electrode. Currently, in the field of pulsed power and microwave irradiation, the key technique is to improve the electron beam sources. Further, the surface treatment of cathode is a major approach to enhance the property of electron beam sources. In our previous works, the introduction of heavier

particles on the surface of cathode can lower the velocity of diode gap closure and improve the uniformity of electron emission (Li *et al.*, 2009b). The surface deposition by plasma torch is also a simple method to introduce the heavier particle on the cathode surface. In this paper, the copper or copper oxide are introduced on the surface of carbon fiber, that is, the heavier particles are deposited by plasma torch, which can provide new prospective for developing pulsed electron beam sources.

ACKNOWLEDGEMENTS

The work was supported by Hong Kong Research Grants Council (RGC) General Research Funds (GRF) nos. CityU112510 and 112212, Natural Science Foundation of China (Granted No. 51101027), and Program for New Century Excellent Talents in Heilongjiang Provincial University. The authors were grateful to Drs. Cheng Cheng and Zhengwei Wu for helpful discussions and suggestions.

REFERENCES

- CHENG, X.-B., LIU, J.-L. & QIAN, B.-L. (2013). Application of high speed frame camera on the intense electron beam accelerator: An overview. *Laser Part. Beams*. doi:10.1017/S0263034613000633.
- FAN, X., LIU, J. & LV, X. (2013). Research on the electromagnetic fields radiating during the operation of intense electron-beam accelerator. *Laser Part. Beams* **31**, 149–154.
- KOLB, J.F., MATTSON, A.M., EDELBLUTE, C.M., HAO, X., MALIK, M.A. & HELLER, L.C. (2012). Cold DC-operated air plasma jet

- for the inactivation of infectious microorganisms. *IEEE Trans. Plasma Sci.* **40**, 3007–3026.
- LI, L., CHANG, L., ZHANG, L., LIU, J., CHEN, G. & WEN, J. (2012). Development mechanism of cathode surface plasmas of high current pulsed electron beam sources for microwave irradiation generation. *Laser Part. Beams* **30**, 541–551.
- LI, L., CHENG, G., ZHANG, L., JI, X., CHANG, L., XU, Q., LIU, L., WEN, J., LI, C. & WAN, H. (2011). Role of the rise rate of beam current in the microwave radiation of vircator. *J. Appl. Phys.* **109**, 074504.
- LI, L., LIU, L., WAN, H., XU, Q., CHENG, G. & WEN, J. (2009a). Surface modification and submicron structure of carbon fibers through high current pulse. *Appl. Surf. Sci.* **255**, 8030–8035.
- LI, L., LIU, L., WEN, J. & LIU, Y. (2009b). Effects of CsI coating of carbon fiber cathodes on the microwave emission from a triode virtual cathode oscillator. *IEEE Trans. Plasma Sci.* **37**, 15–22.
- LI, L., LIU, L., XU, Q., CHANG, L., WAN, H. & WEN, J. (2009c). Propagation of individual plasma spots on cathode surface by high-current discharge process. *Phys. Lett. A* **373**, 1165–1169.
- LI, L., LIU, L., XU, Q., CHEN, G., CHANG, L., WAN, H. & WEN, J. (2009d). Relativistic electron beam source with uniform high-density emitters by pulsed power generators. *Laser Part. Beams* **27**, 335–344.
- LIU, J.-L., ZHANG, H.-B., FAN, Y.-W., HONG, Z.-Q. & FENG, J.-H. (2012). Study of low impedance intense electron-beam accelerator based on magnetic core Tesla transformer. *Laser Part. Beams* **30**, 299–305.
- LU, X., JIANG, Z., XIONG, Q., TANG, Z., HU, X. & PAN, Y. (2008a). An 11 cm long atmospheric pressure cold plasma plume for applications of plasma medicine. *Appl. Phys. Lett.* **92**, 081502.
- LU, X., JIANG, Z., XIONG, Q., TANG, Z. & PAN, Y. (2008b). A single electrode room-temperature plasma jet device for biomedical applications. *Appl. Phys. Lett.* **92**, 151504.
- NOHARA, L.B., FILHO, G.P., NOHARA, E.L., KLEINKE, M.U. & REZENDE, M.C. (2005). Evaluation of carbon fiber surface treated by chemical and cold plasma processes. *Mater. Res.* **8**, 281–286.
- PAN, X., ZHANG, R., PENG, S. & QIU, Y. (2010). Study on the surface modification of PBO fiber under dielectric barrier discharge treatment. *Fibers Polymers* **11**, 372–377.
- PENG, J.-C., LIU, G.-Z., SONG, X.-X. & SU, J.-C. (2011). A high repetitive rate intense electron beam accelerator based on high coupling Tesla transformer. *Laser Part. Beams* **29**, 55–60.
- SARANI, A., NIKIFOROV, A.Y., GEYTER, N.D., MORENT, R. & LEYS, C. (2011). Surface modification of polypropylene with an atmospheric pressure plasma jet sustained in argon and an argon/water vapour mixture. *Appl. Surf. Sci.* **257**, 8737–8741.
- SHAO, T., TARASENKO, V.F., ZHANG, C., BAKSHT, E.K., YAN, P. & SHUT'KO, Y.V. (2012). Repetitive nanosecond-pulse discharge in a highly nonuniform electric field in atmospheric air: X-ray emission and runaway electron generation. *Laser Part. Beams* **30**, 369–378.
- TENG, Y., CHEN, C.H., SUN, H.S.J., SONG, Z.M., XIAO, R.Z. & DU, Z.Y. (2013). Design and efficient operation of a coaxial RBWO. *Laser Part. Beams* **31**, 321–331.
- TIWARI, S., SHARMA, M., PANIER, S., MUTEL, B., MITSCHANG, P. & BIJWE, J. (2011). Influence of cold remote nitrogen oxygen plasma treatment on carbon fabric and its composites with specialty polymers. *J. Mater. Sci.* **46**, 964–974.
- UGENT, A.S., UGENT, A.N., UGENT, N.D.G., UGENT, R.M. & UGENT, C.L. (2011). Surface modification of polypropylene with an atmospheric pressure plasma jet sustained in argon and an argon/water vapour mixture. *Appl. Surf. Sci.* **257**, 8737–8741.
- WU, S., LU, X.P., OSTRIKOV, K., LIU, D. & PAN, Y. (2011). Solitary filamentary structures and nanosecond dynamics in atmospheric-pressure plasmas driven by tailored dc pulses. *Appl. Phys. Lett.* **99**, 161503.
- WU, S., WANG, Z., HUANG, Q., LU, X. & OSTRIKOV, K. (2012). Open-air direct current plasma jet: Scaling up, uniformity, and cellular control. *Phys. Plasmas* **19**, 103503.
- YAN, X., ZOU, F., LU, X.P., HE, G., SHI, M.J., XIONG, Q., GAO, X., XIONG, Z., LI, Y., MA, F.Y., YU, M., WANG, C.D., WANG, Y. & YANG, G. (2009). Effect of the atmospheric pressure nonequilibrium plasmas on the conformational changes of plasmid DNA. *Appl. Phys. Lett.* **95**, 083702.
- YOUSFI, M., HENNAD, A., BENHENNI, M., EICHWALD, O. & MERBAHI, N. (2012). Basic data of ions in He-air mixtures for fluid modeling of low temperature plasma jets. *J. Appl. Phys.* **112**, 043301.
- ZHANG, C., TARASENKO, V.F., SHAO, T., BAKSHT, E.K., BURACHENKO, A.G., YAN, P. & KOSTYRAY, I.D. (2013a). Effect of cathode materials on the generation of runaway electron beams and X-rays in atmospheric pressure air. *Laser Part. Beams* **31**, 353–364.
- ZHANG, Q., SUN, P., FENG, H., WANG, R., LIANG, Y., ZHU, W., BECKER, K.H., ZHANG, J. & FANG, J. (2012a). Assessment of the roles of various inactivation agents in an argon-based direct current atmospheric pressure cold plasma jet. *J. Appl. Phys.* **111**, 123305.
- ZHANG, Y. & LIU, J. (2013b). A new kind of solid-state Marx generator based on transformer type magnetic switches. *Laser Part. Beams* **31**, 239–248.
- ZHANG, Y. & LIU, J.L. (2012b). Impedance matching condition analysis of the multi-filar tape-helix Blumlein PFL with discontinuous dielectrics. *Laser Part. Beams* **30**, 639–650.